Sign reversal of the order parameter in $(Li_{1-x}Fe_x)OHFe_{1-y}Zn_ySe$

Zengyi Du[1][†], Xiong Yang[1][†], Dustin Altenfeld[2][†], Qiangqiang Gu[1][†], Huan Yang[1][†], Ilya Eremin[2], Peter J. Hirschfeld[3]*, Igor I. Mazin[4], Hai Lin[1], Xiyu Zhu[1] and Hai-Hu Wen[1]*

Iron pnictides are the only known family of unconventional high-temperature superconductors besides cuprates. Until recently, it was widely accepted that superconductivity is driven by spin fluctuations and intimately related to the fermiology, specifically, hole and electron pockets separated by the same wavevector that characterizes the dominant spin fluctuations, and supporting order parameters (OP) of opposite signs[1,2]. This picture was questioned after the discovery of intercalated or monolayer form of FeSe-based systems without hole pockets, which seemingly undermines the basis for spin-fluctuation theory and the idea of a sign-changing OP[3-11]. Using the recently proposed phase-sensitive quasiparticle interference technique, here we show that in LiOH-intercalated FeSe compound the OP does change sign, albeit within the electronic pockets. This result unifies the pairing mechanism of iron-based superconductors with or without the hole Fermi pockets and supports the conclusion that spin fluctuations play the key role in electron pairing.

In iron pnictides, it has been widely perceived that superconductivity is driven by spin fluctuations, which supports the sign reversal between order parameters (OP) on the electron and hole pockets[1,2]. The discovery of superconductivity in intercalated or monolayer FeSe at a critical temperature of the order of 40 K rekindled interest in Fe-based superconductivity and sent many theorists back to the drawing board[3-11]. Indeed, the simple, transparent and largely accepted idea of spin fluctuations scattering electron pairs between hole and electron pockets was shaken by the absence of hole pockets in $K_xFe_{2-y}Se_2$. The fact that the superconducting phase was formed by filamentary inclusions in a strongly magnetic matrix[12] spoke against a conventional single-sign s-wave ('s^{++}') pairing[13], and model calculations based on the spin-fluctuation scenario predicted a d-wave state[14,15], which, by symmetry, would have generated gap nodes[16]. On the other hand, later photoemission experiments indicated a nodeless superconducting state[17,18]. After other materials with similar properties were discovered, including $(Li_{1-x}Fe_x)OHFeSe$, which could be synthesized in a single-phase form[6,7], as well as FeSe monolayers[8], it became increasingly clear that superconductivity at ∼40 K and higher is possible without hole pockets.

We do not discuss here possible mechanisms for this superconductivity, nor even whether it may or may not be similar to the superconductivity in Fe-pnictides. Instead, we will concentrate on a phenomenological question of utmost importance: is superconductivity in FeSe derivatives (assuming they all belong to the same class) of a constant OP sign, or does it have a sign-changing OP? The most natural superconductivity of the latter sort is of x^2-y^2 type (where x and y are the directions of the Fe–Fe bonds). As discussed in refs 5,16, crystallographic symmetry-lowering due to the Se positions, and thus doubling of the unit cell, results in this state acquiring gap nodes, although in principle the nodal area may be very small. Moreover, for $K_xFe_{2-y}Se_2$, which exhibits another electron pocket at the zone centre, this should also lead to nodal lines on this pocket, with a typical cosinusoidal angular dependence of the gap. Neither of these effects has been observed[17]. The other type of (truly gapless) sign-changing superconductivity was suggested in ref. 16 and a detailed theory developed by Khodas and Chubukov[19]. They observed that upon accounting for the spin–orbit interaction, the folded electron ellipses anti-cross and form two concentric pockets, of which the inner one is mostly of d_{xz}/d_{yz}, and the outer one of d_{xy} orbital character. This 'bonding–antibonding' scenario[5] postulates that the OP on the inner barrel has one sign, and on the outer barrel the other. The goal of this paper is not to distinguish between the $d_{x^2-y^2}$ and $s^{\pm}$ symmetries, but to eliminate another popular hypothesis, namely that all electron pockets have the same sign of the OP[20]. We emphasize that this question has a principal conceptual importance; it has been widely argued that no high-temperature superconductivity is possible at all, unless the order parameter averages to (nearly) zero over all Fermi surfaces (thus eliminating the effect of the on-site Coulomb repulsion), and it is generally accepted that spin-fluctuation-driven superconductivity necessarily requires a sign-changing order parameter.

Unfortunately, the phase-sensitive probes developed for d-wave cuprates either fail or are more questionable in Fe-based materials. Probes based on Josephson loops with π-contacts, instead of providing a qualitative test, offer only a quantitative probe, since all possible junctions have currents arising from various Fermi surface sheets corresponding to both same-sign and opposite-sign order parameters[21,22]. Quasiparticle interference (QPI) due to scattering from vortex cores is, in principle, phase-sensitive, but the interpretation requires specific models of the superconducting states[23,24]. The technique of identifying bound states formed at a non-magnetic impurity by means of scanning tunnelling microscopy (STM) is more promising, and straightforward to measure. However, here the problem is that it is often hard to prove that the investigated impurities are indeed non-magnetic.

In this paper, we shall report, first, an observation of the above-mentioned bound state, which, notwithstanding the reservations above, strongly suggests a sign-changing order parameter. Second,

[1]Center for Superconducting Physics and Materials, National Laboratory of Solid State Microstructures and Department of Physics, Collaborative Innovation Center for Advanced Microstructures, Nanjing University, Nanjing 210093, China. [2]Institut für Theoretische Physik III, Ruhr-Universität Bochum, D-44801 Bochum, Germany. [3]Department of Physics, University of Florida, Gainesville, Florida 32611, USA. [4]Code 6393, Naval Research Laboratory, Washington DC 20375, USA. [†]These authors contributed equally to this work. *e-mail: pjh@phys.ufl.edu; hhwen@nju.edu.cn
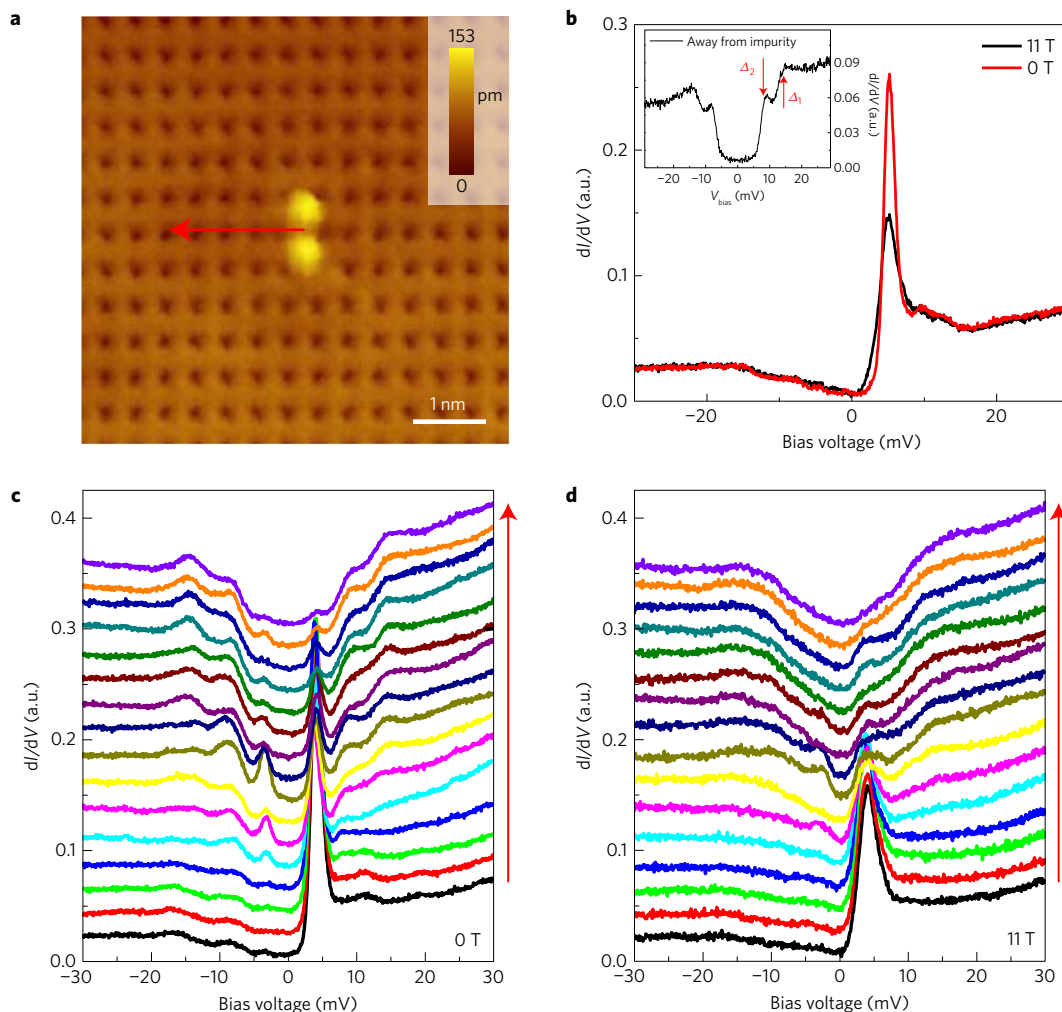
Figure 1 | In-gap resonant states of a non-magnetic impurity. a, STM topography ($V_{bias} = 30$ mV, $I_t = 100$ pA) around a single impurity. The colour bar represents height of the background with units of picometres. **b**, Tunnelling spectra measured at the centre of the defect with a dumbbell shape under $B = 0$ T and 11 T, respectively. The peak position of the impurity bound state does not shift under an 11 T magnetic field, indicating its non-magnetic origin. The inset shows a spectrum measured far away from the impurity site with the two gaps $\Delta_1 = 14$ meV, $\Delta_2 = 8.5$ meV, as marked by the arrows. **c,d**, Tunnelling spectra measured along the red line in **a** at $B = 0$ T and 11 T, respectively. All data shown in this figure were taken at 1.5 K.

we will present a set of QPI measurements, and an analysis that does not rely upon the scattering from vortex cores, a poorly understood process, but upon zero-field integrated quantities, as suggested in ref. 24. As discussed in the following, this analysis involves a minimal number of assumptions and utilizes qualitative differences between the integrated QPI intensities for the sign-changing and sign-conserving QP scatterings. This methodology does not require a separation between intra- and inter-pocket scatterings, and unambiguously identifies the presence of a sign-changing OP. However, this universality comes at a cost; it cannot distinguish between a nodeless $s^{\pm}$ and a nearly nodeless d-state in these systems. This choice has to be made based on separate information.

In this work, we synthesized zinc-doped $(Li_{1-x}Fe_x)OHFeSe$ and measured its material characteristics. The superconducting transition temperature determined using the midpoint of the resistive transition was suppressed from about 37.5 K to about 34.8 K, and the transition width becomes also clearly broadened by Zn-doping. More detailed information is presented as Supplementary Note 1. We have measured the scanning tunnelling spectra (STS) at 1.5 K near a single Fe-substituting impurity in $(Li_{1-x}Fe_x)OHFe_{1-y}Zn_ySe$, and show the results in Fig. 1. The topographic image measured with $V_{bias} = 30$ mV, $I_t = 100$ pA around the single impurity is shown in Fig. 1a. One can see that the impurity exhibits a typical image of a

dumbbell shape with the centre located at the Fe site beneath the top Se layer. This dumbbell shape looks quite similar to the non-magnetic Cu impurities in $NaFe_{0.96}Co_{0.03}Cu_{0.01}As$ (ref. 25), which suggests that the Zn impurity is the origin of the dumbbell shape. This is also supported by the fact that simple counting of the impurities visible in the field of view (FOV) of the STM agrees well with the analysis of X-ray energy dispersive spectrum (EDX). Both yield an approximately 2% Zn/Se atomic ratio in the sample, which is, as expected, less than the nominal 10% concentration. Indeed, we see essentially one type of surface defect with a concentration in the right range, and, while intrinsic defects such as vacancies may or may not occur in a sizeable amount, Zn atoms that exist in the sample must manifest themselves in the STM. Thus, although we cannot definitely identify this impurity as a Zn atom, it seems exceedingly likely. In Fig. 1c,d we show the spatial evolution of the tunnelling spectra along the line shown in Fig. 1a when the magnetic field is zero and 11 T, respectively. One can see that a strong resonant peak appears at about 4.0 meV at the impurity site. When moving away from the impurity, the spectrum recovers a typical shape with two superconducting gaps, similar to the pristine system without Zn (ref. 26). The two gaps $\Delta_1 = 14$ meV and $\Delta_2 = 8.5$ meV, determined here from spectra far away from the impurity (see the inset of Fig. 1b) are also quite close to those in the Zn-free samples[26]. To

illustrate how the magnetic field affects the resonant impurity states, we show in Fig. 1b two selected spectra measured at the impurity site with and without magnetic field. It is clear that the magnetic field suppresses the resonant peak, but does not shift or split the peak.

Both observations are of great importance; the former proves that the peak in question has superconducting origin, and the latter indicates that the impurity is non-magnetic. Indeed, for a magnetic impurity in the Born limit, the energy of a Bogoliubov–de-Gennes (BdG) quasiparticle contains three terms: $H_{qp} = H_0 + g\mu_B \mathbf{S} \cdot \mathbf{H} + \sum_{\mathbf{k},\sigma,\mathbf{k}',\sigma'} J c_{\mathbf{k}\sigma}^+ \boldsymbol{\sigma}_{\sigma,\sigma'} \cdot \mathbf{S} c_{\mathbf{k}'\sigma'}$ (ref. 27). Here the first term H_0 is just the bare energy of a BdG quasiparticle. The second term arises from the interaction between the magnetic moment $\mathbf{S}$ and external field $\mathbf{H}$; g is the Landé factor and μ_B is the Bohr magneton. This term shifts the resonant peak position in a magnetic field. The third term is due to the interaction between the BdG quasiparticles and the local magnetic moment, and will lead to a splitting of the resonant peak. J in this term is the exchange coupling parameter between the BdG quasiparticles and the magnetic moment, while $\boldsymbol{\sigma}_{\sigma,\sigma'}$ denotes the Pauli matrix in spin space and $c_{\mathbf{k}\sigma}^+$ ($c_{\mathbf{k}'\sigma'}$) is the quasiparticle creation (annihilation) operation at momentum $\mathbf{k}(\mathbf{k}')$ with quasiparticle spin $\sigma(\sigma')$. We have monitored more than ten individual 'dumbbell' impurities and have never observed either a shift or splitting of the peak under a magnetic field in the present sample, so we conclude the impurity of this type (presumably Zn atom) is non-magnetic. According to theory[28–30], in multiband superconductors, if the pairing gap has a sign reversal, the non-magnetic impurity with a moderate scattering potential will induce in-gap resonant bound states. For a sign-preserving gap, such as plain s-wave (s^{++}), these bound states are not expected. The observation of the bound state peak at the non-magnetic Zn impurity reflects the sign-reversal gap of the system. Our conclusion that the bound states are associated with Zn atoms seems at odds with ref. 31, which found no such states for Zn atoms dosed onto the surface. We note, however, that the effective potential for a dosed Zn adatom is significantly weaker than for a substitutional Zn impurity. It is highly likely that the former is simply too weak to create a midgap resonance[5,28–30]. This point is discussed further in Supplementary Note 2.

Earlier angle-resolved photoemission[10,11] and STM measurements[26] revealed that the hole Fermi surfaces at the Brillouin centre (Γ point) are absent in (Li$_{1-x}$Fe$_x$)OHFeSe, with only electron pockets at the zone corners. In Fig. 2a, we present a sketch of the Fermi surface topology in the folded (2-Fe) Brillouin zone. Here $\Gamma\tilde{X}$ is the reciprocal vector of the 2-Fe lattice, that is, it is directed along the Fe–Fe square diagonal and equal to $\sqrt{2}\pi/2a$, where a is the Fe–Fe distance.

This Fermi surface geometry generates a rather simple pattern in the QPI image. Since all double pockets around the M-points are equivalent by symmetry (both in the normal and in the superconducting state), there is one roughly circular spot in QPI around the zone centre $\mathbf{q} = 0$, which extends up to approximately $2\mathbf{k}_F$ (where $\mathbf{k}_F$ is the Fermi vector of the outer pocket). This spot is periodically repeated at each reciprocal lattice vector $\mathbf{G}$. Due to tunnelling matrix elements, one expects the spot around $\mathbf{G} = 0$ to be the strongest, the one around $\mathbf{G} = (1,0)$ weaker (labelled as $\mathbf{q}_2$ in Fig. 2b), and the one around $\mathbf{G} = (1,1)$ even weaker ($\mathbf{q}_3$). We will see that this is exactly the picture we observe. The $\mathbf{q}_2$ and $\mathbf{q}_3$ spots do not carry any additional information, being symmetry-equivalent to $\mathbf{q}_1$, so in our analysis we concentrated on the latter. The measured QPI results in a large area can be found in Supplementary Note 3. Note that if the spin–orbit coupling induced gap is sufficiently large, one may, in principle, be able to resolve the $\mathbf{q}_1$ spot into three concentric rings, corresponding to the thresholds of the scattering inside the inner barrel, inside the outer barrel, and the interband scattering. Currently this is beyond attainable resolution, but if in the future, were it to become possible, in the spirit of the discussion below one
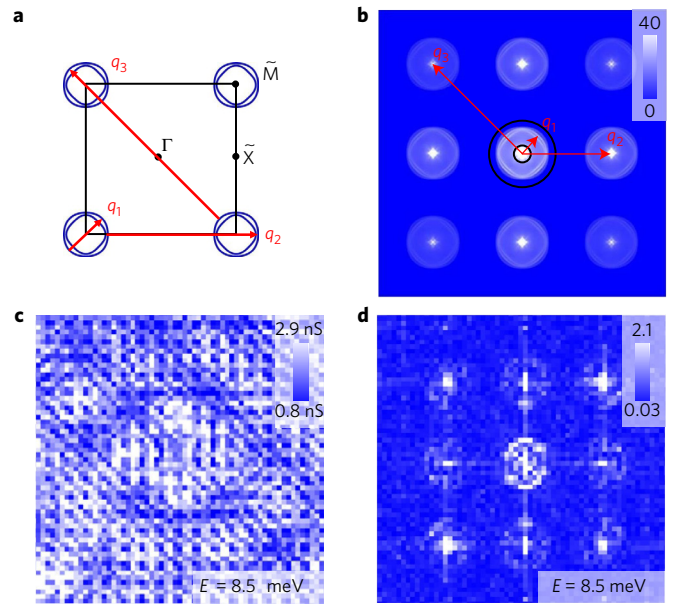

Figure 2 | Quasiparticle interference around the single impurity. a, The schematic Fermi surface of (Li$_{1-x}$Fe$_x$)OHFe$_{1-y}$Zn$_y$Se and three scattering processes in **k** space. The eccentricity of the ellipses is about 0.55. The first Brillouin zone is shown by the solid black line, that is, there are two overlapping pockets per zone. **b**, A sketch showing the QPI structure expected for this Fermi surface; note that $\mathbf{q}_2$ and $\mathbf{q}_3$ differ from $\mathbf{q}_1$ by the first and second reciprocal lattice vector, respectively. Although within the theory employed in this paper they are all equivalent, in reality we expect the signal for larger reciprocal lattice vectors to be weaker, as reflected in this sketch. The sketch is drawn by the self-correlation using the Fermi surface in **a**. **c**, A typical dI/dV map $g(\mathbf{r}, E = 8.5\,\text{meV})$ measured at the smaller superconducting gap energy ($\Delta_2 = 8.5\,\text{meV}$) around the single impurity ($T = 1.5\,\text{K}$). **d**, FT image of **c**, which is qualitatively similar to the sketch shown in **b**.

would be able to distinguish between the bonding–antibonding $s^{\pm}$ and quasi-nodeless d states.

In Fig. 2c, we show a spatial map of the measured differential conductivity $g(\mathbf{r}, E = 8.5\,\text{meV}) = [dI/dV](\mathbf{r}, E = 8.5\,\text{meV})$ at 1.5 K around the single impurity shown in Fig. 1a. One can clearly see patterns generated by the QPI. A Fourier transformation (FT) of Fig. 2c is shown in Fig. 2d, which can be directly compared with the cartoon in Fig. 2b. This validates the Fermi surface topology assumed in Fig. 2a, although our experimental resolution cannot assess the amplitude of the spin–orbital-coupling-induced splitting. We emphasize that to obtain dI/dV on a fine energy mesh, we have used 64×64 grids in the FOV with a single impurity in the centre[32], and measured the STS ($-25\,\text{mV}$ to $25\,\text{mV}$) at each grid point, masking the remainder of the observation window. Then we can rearrange the $g(\mathbf{r}, E)$ data for all the points to create maps with 64×64 pixels at each energy. This new method ensures stability in the following phase-related analysis on the QPI intensity. For details of the measurements and spatial position corrections we refer the reader to Methods and to Supplementary Note 4.

As discussed, in principle we should have three scattering channels and thus three circles around $\mathbf{q} = 0$, as marked in Fig. 3d. Taking into account the orbital character variation around the Fermi surfaces, we observe that these three rings would roughly correspond to the orbital channels $d_{xy} \leftrightarrow d_{xz/yz}$, $d_{xz/yz} \leftrightarrow d_{xz/yz}$, $d_{xy} \leftrightarrow d_{xy}$ for the interband, inner-intraband and outer-intraband scattering, respectively. Near $\mathbf{q} = 0$ we see a bright spot (Fig. 2b) that arises from the very short $\mathbf{q}$-scattering within one single Fermi surface and between the two Fermi surfaces. Due to the existence of
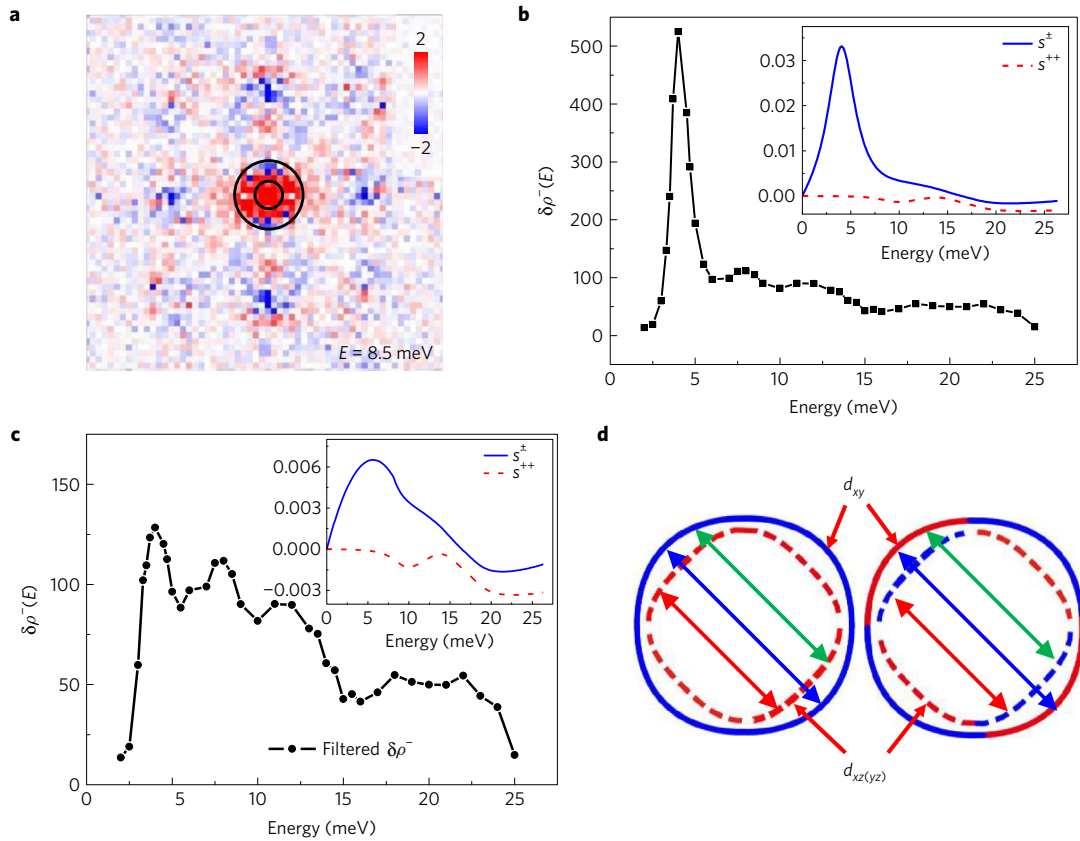
Figure 3 | Determination of sign reversal of the superconducting order parameter. a, The real-part difference of the FT-QPI $\delta\rho^-(\mathbf{q}, E = 8.5\,\text{meV}) = \text{Re}[\rho(\mathbf{q}, E = 8.5\,\text{meV}) - \rho(\mathbf{q}, E = 8.5\,\text{meV})]$. **b**, Integral of $\delta\rho^-(\mathbf{q}, E)$ versus E. The integral range of $|\mathbf{q}|$ is illustrated by the ring in **a** with specified $|\mathbf{q}|$ range, $0.13\pi/a < |\mathbf{q}| < 0.55\pi/a$, with a the Fe–Fe bond length. The strong peak at approximately 4 meV is due to an impurity bound state. The calculated $\delta\rho^-(E)$ is shown in the inset as a blue solid line for $s^{\pm}$ and a red dashed line for s^{++}. **c**, Integral of $\delta\rho^-(\mathbf{q}, E)$ as a function of E with the bound state peak masked out as discussed in the main text. The theoretical results are again presented as an inset, with the same convention. **d**, Sketch of the Fermi surface electronic pockets, illustrating two possible sign-reversal scenarios; the blue and red colours represent the opposite signs of the order parameter. The red and blue scattering vectors span same-sign order parameters, and the green ones the opposite-sign ones, in both cases.

significant background QPI intensity in the region close to $\mathbf{q} = 0$ we shall not consider this part as relevant for the analysis.

Some of us have recently proposed[24] a new methodology for robust determination of possible order parameter sign reversal, using QPI from a single non-magnetic impurity. The central prediction is that the anti-symmetrized intensity of the real part of the FT-QPI is proportional to

$$\delta\rho^-(E) = \sum_{q \in A} \text{Re}[\rho(\mathbf{q}, +E) - \rho(\mathbf{q}, -E)]$$

$$\propto U \text{Im} \frac{E^2 - \Delta_1 \Delta_2}{\sqrt{E^2 - \Delta_1^2}\sqrt{E^2 - \Delta_2^2}} \quad (1)$$

for a weak scatterer, and the structure of this result is universal in the sense that it does not depend qualitatively on the strength of the scattering and the details of the electronic structure[24]. Here Δ_1 and Δ_2 are the two gaps associated with the two bands, U is a scalar scattering potential, A represents an area in $\mathbf{q}$-space containing gap-sign-changing scattering vectors, and $\rho(\mathbf{q}, E)$ represents the FT-QPI, which is the FT of the spatial map of the differential conductivity $g(\mathbf{r}, E)$. The prediction for an $s^{\pm}$ pairing state is that this quantity, $\delta\rho^-(E)$, at an energy between the two gaps will be coherently enhanced and hence does not change sign with $E > 0$, while for an s^{++} case, this quantity is generally small, with an alternating sign between the two gaps. We have calculated $\delta\rho^-(E)$

from our measured data and show it in Fig. 3a. The phase shift has been corrected by taking the impurity as the origin point of the QPI image before the FT, as demonstrated in ref. 32. The details can be found in Supplementary Note 4. To get an enhanced signal/noise ratio, we have integrated the data within the ring defined by $0.13\pi/a < |\mathbf{q}| < 0.55\pi/a$, with a being the Fe–Fe bond length. This area is determined by simulation, with the requirement that the small-q scattering near $\mathbf{q} = 0$ can be effectively neglected. This is explained in Supplementary Note 5. The energy dependence of $\delta\rho^-(E)$ is presented in the main panel of Fig. 3b. One can see a sharp peak at about 4.0 mV, which corresponds to an impurity resonance (see Fig. 1b). This peak is unrelated to the phase-dependent analysis of QPI and needs to be removed prior to further analysis. To illustrate the energy dependence of the $\delta\rho^-$ image, we present a movie with a series of $\delta\rho^-$ images as a function of energy (see Supplementary Movie 1). As one can see, at some low energies, an artificial asymmetry of $\delta\rho^-(\mathbf{q}, E)$ is observed. Above the smaller gap, this asymmetry becomes weaker and finally vanishes; the energies between the two gaps, namely between 8.5 to 14 meV, which are most relevant to our analysis, are very little affected by this asymmetry.

To eliminate the effect of the bound state, we have masked the central part of the two-dimensional (2D) map of dI/dV with a circle of $R = 3$ pixels radius (29 pixels around the defect) by assuming a parabolic relation $\delta\rho(E) = AE^2 + B|E|$ in the energy window from 3 to 5.5 meV. The details of this masking can be found in Supplementary Note 6. The calculated experimental data

of $\delta\rho^-(E)$ after this masking are shown in the main panel of Fig. 3c. The masking procedures for experimental data and theoretical calculations are given in Supplementary Notes 6 and 7.

We are now ready to compare the experimental data with the theoretical predictions of ref. 24. To begin with, we have simulated the results of the unmasked processing presented in Fig. 3b, by integrating the simulated $\delta\rho^-(\mathbf{q}, E)$ over the same ring in $\mathbf{q}$-space. For parameters we used $E_{imp} = 4.0$ meV, $\Delta_2 = 8.5$ meV, and $\Delta_1 = 14$ meV. The calculated result is shown in the inset of Fig. 3b (more details of the calculations are presented in Methods and in Supplementary Note 6). We immediately observe that the $s^{\pm}$ model reproduces the essential features of the experimental data. One can, however, argue that in the $s^{\pm}$ case the spectral weight is dominated by the impurity resonance. To address this point, we present in Fig. 3c the $\delta\rho^-(E)$ obtained after the removal of the resonance, as discussed above, and, in the inset, the calculated $\delta\rho^-(E)$ subjected to the same masking procedure. Again, we see a qualitative difference between the two cases, with only the $s^{\pm}$ calculation reproducing the experimental spectrum (and, in fact, reproducing it very well). This gives us strong confidence that gaps change sign between two or more Fermi surface sheets, as shown in Fig. 3d. Note that our analysis is not based on a detailed, model-dependent comparison between the measurements and simulations, but upon a very qualitative analysis, and the observed agreement hinges exclusively on the fact that the assumed pairing state has a sign-changing order parameter. A new round of measurements has been repeated on the same impurity later, and the resulting energy dependence of the anti-symmetrized FT-QPI spectra is quite similar to the data presented here. In addition, a new impurity in the same sample was chosen to perform the control experiment, with a very similar result. All these results are described in Supplementary Note 8 and Supplementary Figs 7 and 8. The similar results from the control experiments lend strong support to the analysis and conclusions presented in the paper.

To summarize, we have shown, based on both the observation of an in-gap impurity state for the non-magnetic impurities, and a novel theoretical analysis of quasiparticle interference data, that the order parameter in intercalated FeSe, specifically in $(Li_{1-x}Fe_x)OHFe_{1-y}Zn_ySe$, alternates sign, either between the Fermi surface sheets, or within individual sheets, as illustrated in Fig. 3d. Furthermore, the order parameter sign must affect a considerable fraction of the scattering processes, meaning that the two opposite signs are roughly balanced. This puts severe restrictions on the available scenarios. Of those proposed so far, two satisfy this experiment: the bonding–antibonding s-wave state or a nearly nodeless d-wave state, as discussed, for instance, in ref. 5. At present, our results do not allow us to distinguish between the two. The latter has an advantage of having a clear candidate for pairing glue, namely spin fluctuations resulting from inter-pocket nesting in the unfolded zone (note that such fluctuations were observed, at $q = \{\pi, \pi/2\}$ (refs 33–35) and calculated, at $q = \{\pi, 0.625\pi\}$ (ref. 14) in $K_xFe_{2-y}Se_2$ or other intercalated system, which would have naturally led to a state depicted in Fig. 3d(right). A principal problem with this option, however, is that in the related $K_xFe_{2-y}Se_2$ it is incompatible with the nodeless Γ-pocket gap[17], so one has to assume different pairing symmetry in these otherwise fairly similar materials, and the symmetry-required gap nodes at the points where the red and blue lines intersect in Fig. 3d(right), must be very steep, that is, $d\Delta/dk \gg \Delta/k_F$. The bonding–antibonding $s^{\pm}$ scenario, on the other hand, has an additional advantage in the sense that in this case the sign of the order parameter naturally follows the orbital character of the bands, with the xy orbitals carrying one sign, and the xz/yz orbitals the other (Fig. 3d). This greatly narrows the selection from various possible scenarios in the related systems[36]. We must emphasize that our present work is based on a novel theoretical proposal[24]. It would be interesting and important to

do the same experiment and analysis on a system with different gaps having the same sign. A good candidate for this control experiment would be LiFeAs, with its good surface quality and well-separated hole pockets. But in that case it is not entirely clear whether all hole pockets have the same sign of the order parameter. The optimally doped $Ba_{1-x}K_xFe_2As_2$ may be another good system to try this idea, supposing that the surface is clean enough. Our observation of sign-reversing gaps in this electron-Fermi-pocket-only system suggests a universality of the pairing mechanism in the Fe-based superconductors.

Methods

Methods, including statements of data availability and any associated accession codes and references, are available in the online version of this paper.

References

1. Mazin, I. I., Singh, D. J., Johannes, M. D. & Du, M. H. Unconventional superconductivity with a sign reversal in the order parameter of LaFeAsO$_{1-x}$F$_x$. *Phys. Rev. Lett.* **101,** 057003 (2008).
2. Kuroki, K. *et al.* Unconventional pairing originating from the disconnected Fermi surfaces of superconducting LaFeAsO$_{1-x}$F$_x$. *Phys. Rev. Lett.* **101,** 087004 (2008).
3. Guo, J. G. *et al.* Superconductivity in the iron selenide K$_x$Fe$_2$Se$_2$ ($0 < x < 1.0$). *Phys. Rev. B* **82,** 180520 (2010).
4. Fang, M. H. *et al.* Fe-based superconductivity with $T_c = 31$ K bordering an antiferromagnetic insulator in (Tl,K)Fe$_x$Se$_2$. *Europhys. Lett.* **94,** 27009 (2011).
5. Hirschfeld, P. J., Korshunov, M. M. & Mazin, I. I. Gap symmetry and structure of Fe-based superconductors. *Rep. Prog. Phys.* **74,** 124508 (2011).
6. Lu, X. F. *et al.* Coexistence of superconductivity and antiferromagnetism in (Li$_{0.8}$Fe$_{0.2}$)OHFeSe. *Nat. Mater.* **14,** 325–329 (2015).
7. Pachmayr, U. *et al.* Coexistence of 3d-ferromagnetism and superconductivity in [(Li$_{1-x}$Fe$_x$)OH](Fe$_{1-y}$Li$_y$)Se. *Angew. Chem. Int. Ed.* **54,** 293–297 (2015).
8. Wang, Q. Y. *et al.* Interface-induced high-temperature superconductivity in single unit-cell FeSe films on SrTiO$_3$. *Chin. Phys. Lett.* **29,** 037402 (2012).
9. Miyata, Y., Nakayama, K., Sugawara, K., Sato, T. & Takahashi, T. High-temperature superconductivity in potassium-coated multilayer FeSe thin films. *Nat. Mater.* **14,** 775–779 (2015).
10. Niu, X. H. *et al.* Surface electronic structure and isotropic superconducting gap in (Li$_{0.8}$Fe$_{0.2}$)OHFeSe. *Phys. Rev. B* **92,** 060504 (2015).
11. Zhao, L. *et al.* Common electronic origin of superconductivity in (Li, Fe)OHFeSe bulk superconductor and single-layer FeSe/SrTiO$_3$ films. *Nat. Commun.* **7,** 10608 (2016).
12. Ding, X. X. *et al.* Influence of microstructure on superconductivity in K$_x$Fe$_{2-y}$Se$_2$ and evidence for a new parent phase K$_2$Fe$_7$Se$_8$. *Nat. Commun.* **4,** 1897 (2013).
13. Mazin, I. I. Iron superconductivity weathers another storm. *Physics* **4,** 26 (2011).
14. Maier, T. A., Graser, S., Hirschfeld, P. J. & Scalapino, D. J. d-wave pairing from spin fluctuations in the KFe$_2$Se$_2$ superconductors. *Phys. Rev. B* **83,** 100515 (2011).
15. Wang, F. *et al.* The electron pairing of K$_x$Fe$_{2-y}$Se$_2$. *Europhys. Lett.* **93,** 57003 (2011).
16. Mazin, I. I. Symmetry analysis of possible superconducting states in K$_x$Fe$_y$Se$_2$ superconductors. *Phys. Rev. B* **84,** 024529 (2011).
17. Mu, X. *et al.* Evidence for an s-wave superconducting gap in K$_x$Fe$_{2-y}$Se$_2$ from angle-resolved photoemission. *Phys. Rev. B* **85,** 220504 (2012).
18. Zhao, L. *et al.* Common Fermi-surface topology and nodeless superconducting gap of K$_{0.68}$Fe$_{1.79}$Se$_2$ and (Tl$_{0.45}$K$_{0.34}$)Fe$_{1.84}$Se$_2$ superconductors revealed via angle-resolved photoemission. *Phys. Rev. B* **83,** 140508 (2011).
19. Khodas, M. & Chubukov, A. V. Interpocket pairing and gap symmetry in Fe-based superconductors with only electron pockets. *Phys. Rev. Lett.* **108,** 247003 (2012).
20. Onari, S. & Kontani, H. Self-consistent vertex correction analysis for iron-based superconductors: mechanism of Coulomb interaction-driven orbital fluctuations. *Phys. Rev. Lett.* **109,** 137001 (2012).
21. Golubov, A. A. & Mazin, I. I. Designing phase-sensitive tests for Fe-based superconductors. *Appl. Phys. Lett.* **102,** 032601 (2013).

22. Parker, D. & Mazin, I. I. Possible phase-sensitive tests of pairing symmetry in pnictide superconductors. *Phys. Rev. Lett.* **102**, 227007 (2009).

23. Hanaguri, T., Niitaka, S., Kuroki, K. & Takagi, H. Unconventional *s*-wave superconductivity in Fe(Se,Te). *Science* **328**, 474–476 (2010).

24. Hirschfeld, P. J., Altenfeld, D., Eremin, I. & Mazin, I. I. Robust determination of superconducting gap sign changes via quasiparticle interference. *Phys. Rev. B* **92**, 184513 (2015).

25. Yang, H. et al. In-gap quasiparticle excitations induced by non-magnetic Cu impurities in Na(Fe$_{0.96}$Co$_{0.03}$Cu$_{0.01}$)As revealed by scanning tunnelling spectroscopy. *Nat. Commun.* **4**, 2749 (2013).

26. Du, Z. Y. et al. Scrutinizing the double superconducting gaps and strong coupling pairing in (Li$_{1-x}$Fe$_x$)OHFeSe. *Nat. Commun.* **7**, 10565 (2016).

27. Balatsky, A. V., Vekhter, I. & Zhu, J.-X. Impurity-induced states in conventional and unconventional superconductors. *Rev. Mod. Phys.* **78**, 373–433 (2006).

28. Kariyado, T. & Ogata, M. Single impurity problem in iron-pnictide superconductors. *J. Phys. Soc. Jpn.* **79**, 083704 (2010).

29. Bang, Y., Choi, H. Y. & Won, H. Impurity effects on the $\pm$s-wave state of the iron-based superconductors. *Phys. Rev. B* **79**, 054529 (2009).

30. Beaird, R., Vekhter, I. & Zhu, J. X. Impurity states in multiband *s*-wave superconductors: analysis of iron pnictides. *Phys. Rev. B* **86**, 140507 (2012).

31. Yan, Y. J. et al. Surface electronic structure and evidence of plain s-wave superconductivity in (Li$_{0.8}$Fe$_{0.2}$)OHFeSe. *Phys. Rev. B* **94**, 134502 (2016).

32. Sprau, P. O. et al. Discovery of orbital-selective Cooper pairing in FeSe. *Science* **357**, 75–80 (2017).

33. Davies, N. R. et al. Spin resonance in the superconducting state of Li$_{1-x}$Fe$_x$ODFe$_{1-y}$Se observed by neutron spectroscopy. *Phys. Rev. B* **94**, 144503 (2016).

34. Pan, B. Y. et al. Structure of spin excitations in heavily electron-doped Li$_{0.8}$Fe$_{0.2}$ODFeSe superconductors. *Nat. Commun.* **8**, 123 (2017).

35. Park, J. T. et al. Magnetic resonant mode in the low-energy spin-excitation spectrum of superconducting Rb$_2$Fe$_4$Se$_5$ single crystals. *Phys. Rev. Lett.* **107**, 177005 (2011).

36. Huang, D. & Hoffman, J. E. Monolayer FeSe on SrTiO$_3$. *Annu. Rev. Condens. Matter Phys.* **8**, 311–336 (2017).

Author contributions

The low-temperature STS measurements were performed by Z.D., X.Y., Q.G. and H.Y. Data analysis was done by Z.D., X.Y., Q.G., H.Y. and H.-H.W. The samples were grown by H.L. and X.Y.Z. The theoretical calculations were done by D.A. and I.E. All authors contributed to the writing of the paper, with P.H., I.I.M. and H.-H.W. responsible for the final text. H.-H.W. coordinated the whole work. All authors have discussed the results and the interpretations.

Additional information

Supplementary information is available in the online version of the paper. Reprints and permissions information is available online at www.nature.com/reprints. Publisher's note: Springer Nature remains neutral with regard to jurisdictional claims in published maps and institutional affiliations. Correspondence and requests for materials should be addressed to P.J.H. or H.-H.W.

Competing financial interests

The authors declare no competing financial interests.

Methods

Sample synthesis. $(Li_{1-x}Fe_x)OHFe_{1-y}Zn_ySe$ single crystals were synthesized by the hydrothermal ion-exchange method. Firstly, single crystals with the nominal composition $K_{0.8}(Fe_{0.9}Zn_{0.1})_{2-x}Se_2$ were manufactured in advance by the same self-flux method that had been used to synthesize pristine $K_{0.8}Fe_{2-x}Se_2$ single crystals. Afterwards, 10 ml deionized water, 5 g LiOH (J&K, 99% purity), 0.6 g iron powder (Aladdin Industrial, 99% purity), and 0.3 g selenourea (Alfa Aesar, 99% purity) were added to a 50 ml Teflon-lined stainless-steel autoclave. After complete mixing, some pieces of $K_{0.8}(Fe_{0.9}Zn_{0.1})_{2-x}Se_2$ single crystals were added into the mixture. Then, the autoclave was sealed and heated up to $120\,^{\circ}C$, and the temperature was maintained for 40 to 50 h. Finally, the $(Li_{1-x}Fe_x)OHFe_{1-y}Zn_ySe$ single crystals were obtained by cooling the autoclave to room temperature. An X-ray energy dispersive spectrum (EDS) analysis using scanning electronic microscopy suggests that the composition ratio of Fe:Se is about 1.2:1, and the ratio of Zn:Se is about 2%, indicating partial substitution of Zn at the Fe sites in the Fe layer. The characteristics of the sample are presented as Supplementary Note 1.

STM/STS measurements. The STM/STS measurements were carried out in a scanning tunnelling microscope (USM-1300, Unisoku) with an ultrahigh vacuum, low temperature and high magnetic field. The samples were cleaved in an ultrahigh vacuum with a base pressure of about 1×10^{-10} torr. Tungsten tips were used during all the STM/STS measurements. To raise the signal-to-noise ratio, a typical lock-in technique was used with an a.c. modulation of 0.4 mV at 987.5 Hz.

Differential conductivity measurements on a dense energy mesh in real space. To eliminate uncertainties during the QPI analysis, we have measured the full spectrum using a dense energy mesh at each point in the real space. Firstly, we choose an area of 6 nm × 6 nm with a single impurity sitting at the centre of the image. Then, we divide the scanning area into 64 × 64 pixels and measure tunnelling spectra in the voltage window from −25 mV to 25 mV with the same set-point at each position. Then the 2D mapping images of the differential conductivity at different energies are derived from the tunnelling spectrum at each point.

Theoretical calculations. To describe the FT-QPI result, we employ a two-band tight-binding parametrization of the two elliptic electron pockets of the Fermi surface, rotated with respect to each other by $90°$ on the Fermi surface, as described in Supplementary Note 7. The scattering of quasiparticles by a non-magnetic impurity, measured in the FT-QPI, was calculated as a correction to the local density of states (LDOS), using the standard T-matrix approach describing multiple scattering by a single impurity. In particular, we compute the anti-symmetrized correction to the LDOS

$$\delta\rho^-(E) = \frac{1}{2}\mathrm{Tr}\,\mathrm{Im}\sum_{\mathbf{k},\mathbf{q},\mu,\nu}\tau_3 G_\mu^0(\mathbf{k},E)t_{\mu\nu}(E)G_\nu^0(\mathbf{k},E) \quad (2)$$

Here, $G_\mu^0(\mathbf{k},E) = -(iE\tau_0 + \varepsilon_\mu(\mathbf{k})\tau_3 + \Delta_\mu\tau_1)/(E^2 + \Delta_\mu^2 + \varepsilon_\mu^2(\mathbf{k}))$ refers to the Nambu–Gor'kov Green's function for the band μ, and τ_i is the ith Pauli matrix. $\varepsilon_\mu(\mathbf{k})$ and Δ_μ refer to the quasiparticle energy and superconducting gap, respectively, of the corresponding band. The T-matrix for the multiple scattering by a single impurity in the band and Nambu–Gor'kov space is defined as

$$\hat{t}(E) = \left[1 - \hat{U}\tau_3 \sum_{\mathbf{k}}\hat{G}(\mathbf{k},E)\right]^{-1}\tau_3\hat{U} \quad (3)$$

where $U_{\mu\mu} = U_{\mathrm{intra}}\tau_0$ and $U_{\mu\nu} = U_{\mathrm{inter}}\tau_0$ are the intra- and interband impurity scattering strengths, respectively.

Data availability. The data that support the plots within this paper and other findings of this study are available from the corresponding author upon reasonable request.

Sign Reversal of the Order Parameter in $(Li_{1-x}Fe_x)OHFe_{1-y}Zn_ySe$

Zengyi Du[1*], Xiong Yang[1*], Dustin Altenfeld[2*], Qiangqiang Gu[1*], Huan Yang[1*], Ilya

Eremin[2], Peter J. Hirschfeld[3†], Igor I. Mazin[4], Hai Lin[1], Xiyu Zhu[1], and Hai-Hu Wen[1†]

1. Sample characterization

To check the quality of $(Li_{1-x}Fe_x)OHFe_{1-y}Zn_ySe$ sample with the nominal doping of y

= 10%, we have measured the temperature dependence of resistivity and DC

magnetization. The EDS/EDX analysis shows that the actual content of Zn in the

sample is around 2%. The resistivity measurements were carried out in a PPMS-16T

(Quantum Design) with the standard four-probe method. The DC magnetization

measurement was carried out with a SQUID-VSM-7T (Quantum Design).

Figure S1a shows the temperature dependence of zero-field-cooled and

field-cooled magnetization in $(Li_{1-x}Fe_x)OHFe_{1-y}Zn_ySe$ and $(Li_{1-x}Fe_x)OHFeSe$ samples

measured in the magnetic field of 20 Oe. The superconducting transition determined

by the DC magnetization shows a much wider transition for the Zn doped sample.

Figure S1b shows the temperature dependence of resistivity for a pristine sample

$(Li_{1-x}Fe_x)OHFeSe$ and a zinc doped $(Li_{1-x}Fe_x)OHFe_{1-y}Zn_ySe$ sample. The superconducting

transition width determined from resistivity changes from 2.3 K in $(Li_{1-x}Fe_x)OHFeSe$ to

4 K in $(Li_{1-x}Fe_x)OHFe_{1-y}Zn_ySe$, the superconducting transition temperature determined

by the midpoint of the resistive transition is also suppressed from about 37.5 K to

about 34.8 K by Zn-doping. The normal state residual resistivity ρ_0 is determined

through a linear fit to the normal-state data at high temperatures. We can see that ρ_0

increases by about 3 times in $(Li_{1-x}Fe_x)OHFe_{1-y}Zn_ySe$ compared with that in the

pristine sample. The enhancement of residual resistivity ρ_0, suppression of T_c and

broadened transition width in $(Li_{1-x}Fe_x)OHFe_{1-y}Zn_ySe$ all prove the presence of zinc

doping in the sample.
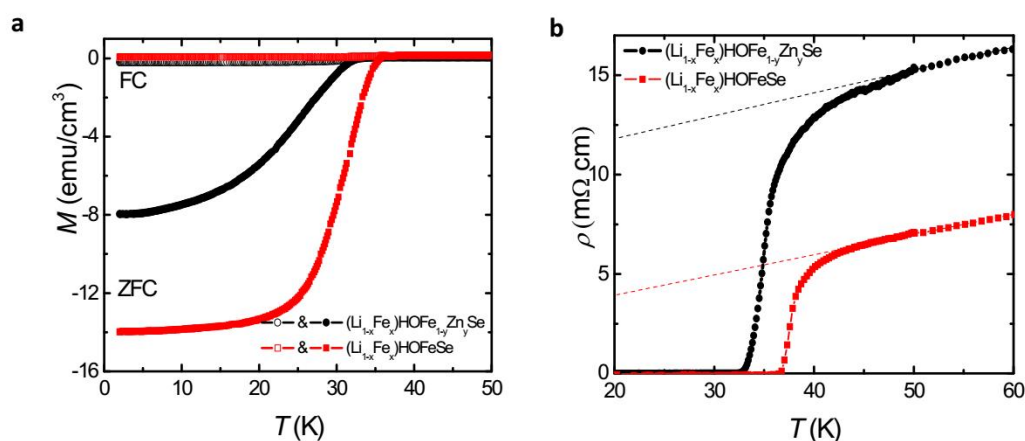
Figure S1 | Superconducting transition of $(Li_{1-x}Fe_x)OHFe_{1-y}Zn_ySe$ and $(Li_{1-x}Fe_x)OHFeSe$ samples. a, Temperature dependence of DC magnetization measured with the zero-field-cooled (ZFC, filled symbols) and field-cooled (FC, open symbols) modes at 20 Oe in $(Li_{1-x}Fe_x)OHFe_{1-y}Zn_ySe$ and $(Li_{1-x}Fe_x)OHFeSe$. **b,** Temperature dependence of resistivity for the $(Li_{1-x}Fe_x)OHFe_{1-y}Zn_ySe$ (circles) and $(Li_{1-x}Fe_x)OHFeSe$ (squares) samples.

2. Magnetic impurities in $(Li_{1-x}Fe_x)OHFeSe$

To contrast our results to those in samples without Zn-doping, we show here

resonant states induced by magnetic impurities in (Li$_{1-x}$Fe$_x$)OHFeSe. About half of the investigated defects in (Li$_{1-x}$Fe$_x$)OHFeSe behave as non-magnetic ones, i.e., the resonant peak position is independent of magnetic field up to 11 T. However, the situation is different for the other half. An example of such magnetic impurities is shown in Fig. S2. This impurity is also residing at an Fe site in the FeSe layer. Now, two strong separated resonance peaks are observed, located at +3.0 and +6.1 mV, respectively. After a magnetic field of 11 T is applied, the peaks move to +4.5 and +7.3 mV, representing shifts of 1.5 and 1.2 mV. The calculated magnetic moment for this impurity is about $M = 0.96\mu_B$, based on the formula $\Delta E = MH$. While the nature of these defects is unclear, we can speculate that the magnetic ones derive from Fe vacancies, and the nonmagnetic ones are probably the Li$^+$ ions substituting Fe^{2+} (which have nearly the same ionic radii). It should be noted that the resonance peak at about -6 mV also moves away from zero with magnetic field, which is similar to the situation with Fe-vacancies in K$_x$Fe$_{2-y}$Se$_2$ [ref. S1]. Although almost half of the impurities in pristine (Li$_{1-x}$Fe$_x$)OHFeSe single crystals behave as magnetic, we have not found any such impurities in (Li$_{1-x}$Fe$_x$)OHFe$_{1-y}$Zn$_y$Se samples (consistent with the hypothesis above, we speculate that the Zn impurities fill up Fe vacancies that could generate local magnetism). This strongly suggests that the impurities investigated in present work are non-magnetic.
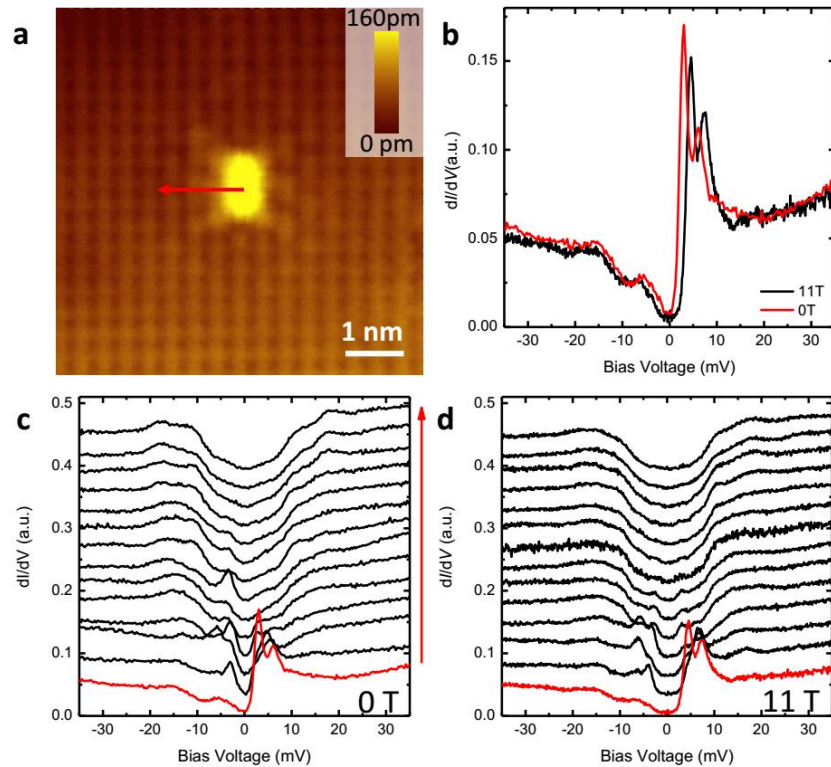
Figure S2 | In-gap resonant states induced by a magnetic impurity in (Li$_{1-x}$Fe$_x$)OHFeSe. a, STM topography (V_{bias} = 30 mV, I_t = 100 pA) of a single impurity in (Li$_{1-x}$Fe$_x$)OHFeSe without Zn-doping. The color bar represents height of the background with unit of pico-meter. **b,** Tunneling spectra measured at the center of the impurity under B = 0 T and 11 T respectively. **c, d** Spectra measured along the red line in **a** at B = 0 T and 11 T.

3. QPI measurement in large area

To determine the electronic structure of the Zn-doped (Li$_{1-x}$Fe$_x$)OHFe$_{1-y}$Zn$_y$Se sample, we have measured the QPI in a large area, which enables us to determine the Fermi surface with high resolution. We show the topography image in Fig. S3a. This area contains many impurities. Figure S3b shows the density of states mapping

at the energy of -13 meV. One can see the standing waves around impurities very clearly. Then we perform the Fourier transformation of the map shown in Fig. S3b. The obtained FT-QPI image is shown in Fig. S3c. The resultant FT-QPI pattern looks almost the same as that measured on the pristine samples (Ref. 26). Also, the measured QPI pattern is comparable to the simulation result shown in Fig. S3d.
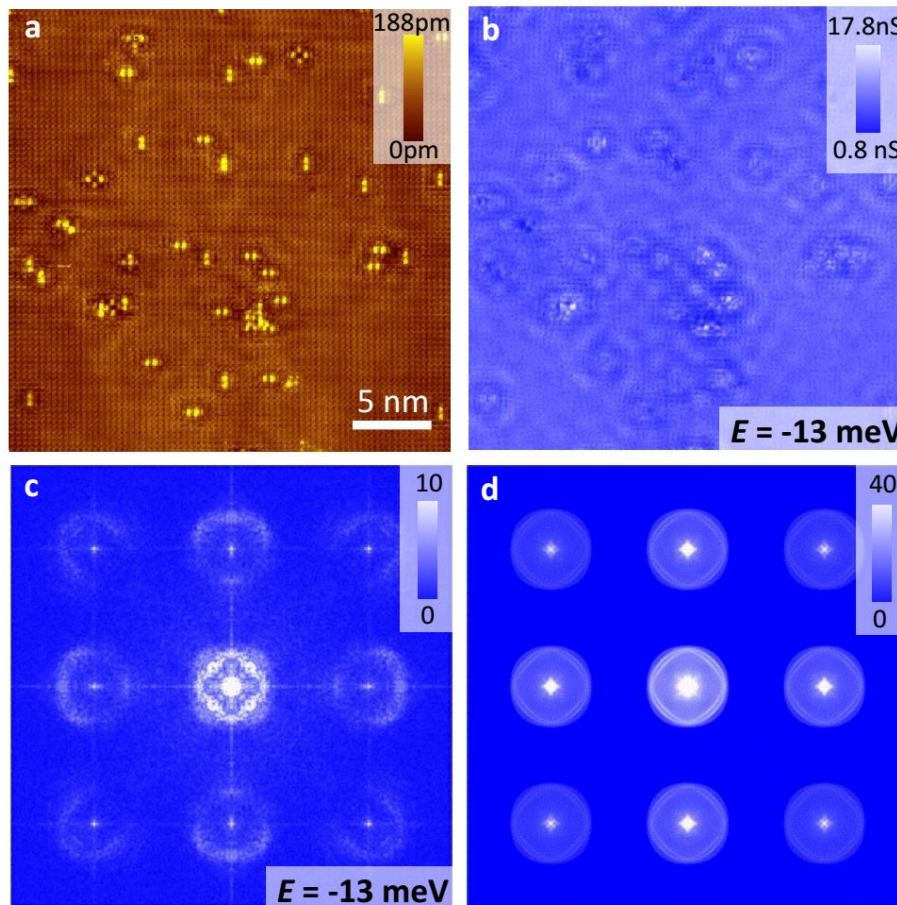

Figure S3 | QPI measurement on $(Li_{1-x}Fe_x)OHFe_{1-y}Zn_ySe$ sample in a large area. **a,** The topography of the Zn-doped sample in a 28 nm $\times$ 28 nm area with many impurities. The setting conditions for measuring the image are V_{bias} = 30 mV and I_t = 50 pA with 256 $\times$ 256 pixels. The color bar represents the height of the background

with unit of pico-meter. **b**, The QPI image at the energy of -13 meV. **c**, The FT-QPI intensity $\rho(q, E = -13\,\text{meV})$ obtained by performing the Fourier transformation on **b**. The image is fourfold symmetrized to enhance the signal. **d**, The simulation result of the QPI pattern (with the intensity reduced for the finite reciprocal lattice vectors by factors of 2 and 4.)

4. Phase correction and extracting the real-part of the anti-symmetrized FT-QPI spectra

If an impurity is located away from the origin, an additional phase term in **q**-space appears, obscuring the behavior of the Fourier transformation: $\text{FT}[f(\mathbf{r} - \mathbf{r_0})] = e^{-i\mathbf{q}\cdot\mathbf{r_0}}\text{FT}[f(\mathbf{r})]$. To avoid this situation, a phase correction is required. This procedure is well described in Ref. S2. The technique used is as follows. We first center our image roughly at the impurity site, and take this point at the origin, then measure the spatial conductance map with 64×64 pixels for each energy (examples are shown in Figs. S4a and c). In order to put the impurity site as the real origin, we remove some edge pixels, and end up with an array of 60×60 pixels, as shown in Figs. S4b and d. This is then taken as the final image and subjected to the Fourier transformation. The result is anti-symmetrized with respect to the bias E, and we obtain the tunneling conductance $\delta\rho^-(\mathbf{q}, E)$ shown in Fig. S4f.
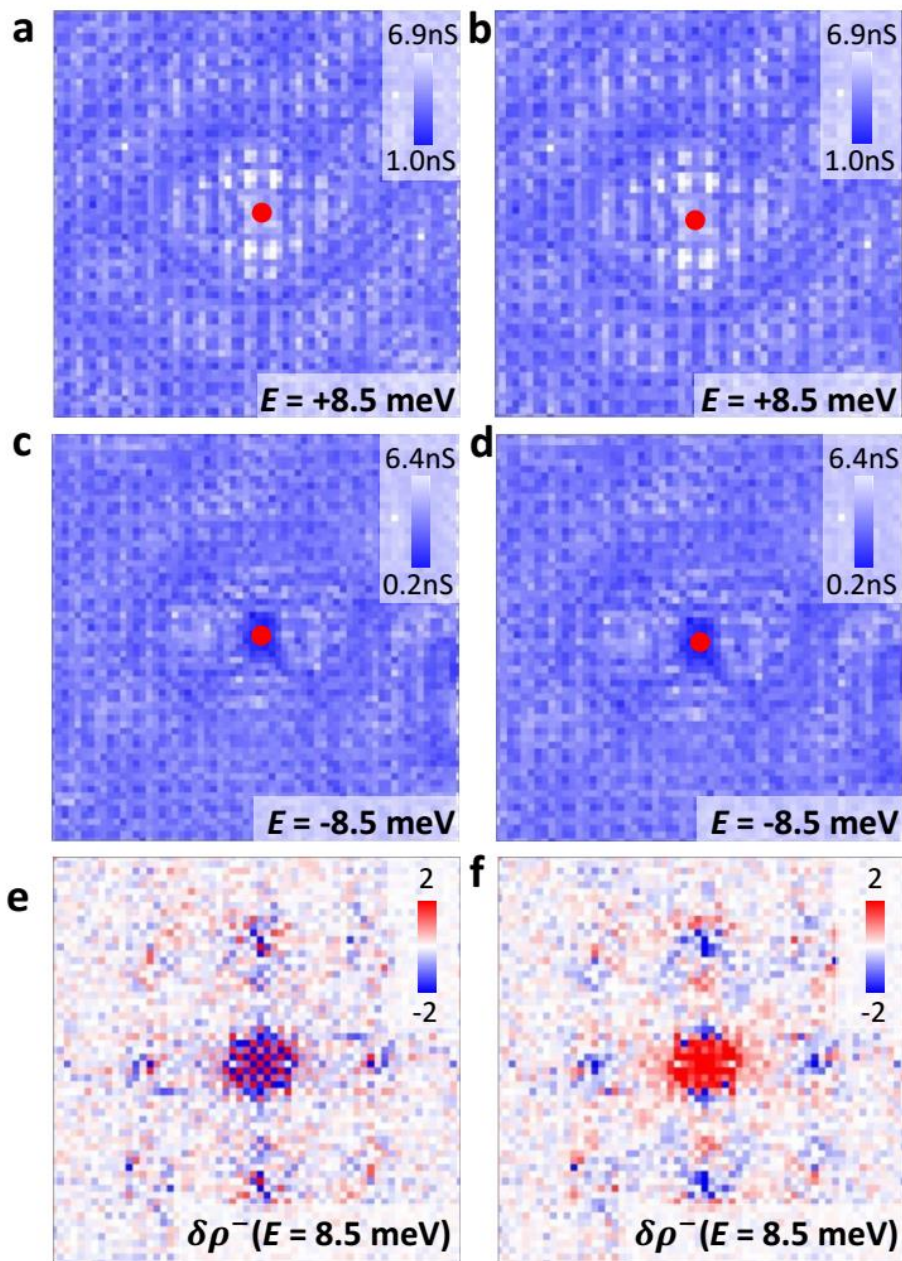
Figure S4 | Phase correction and algorithm for extracting the antisymmetric part of the FT-QPI. a, c, Measured $g(\mathbf{r}, E)$ around a single impurity for $E = 8.5, -8.5$ meV. **b, d,** Edge pixels removed to ensure that the impurity is located exactly at the center of the image. **e,** Antisymmetrized real-part of FT-QPI is calculated as $\delta\rho^-(\mathbf{q}, E = 8.5 \text{ meV}) = \text{Re}[\rho(\mathbf{q}, E = +8.5 \text{ meV}) - \rho(\mathbf{q}, E = -8.5 \text{ meV})]$. The difference

between **e** (no edge points removed) and **f** illustrates the importance of precise selection of the FT origin.

5. Selection of the integration range in q-space for calculating $\delta\rho^-$

At small q vectors we observe a parasitic signal due to disorder, which steals the spectral weight from the **q** = 0 Bragg peak. We solve this problem by carefully selecting the integration area, as discussed below: First, we simulate the inter- and intra-pocket scatterings (the joint density of states, JDOS) and show them in Figs. S5a and b, by using the model Fermi surface shown in Fig. S5c. In Fig. S5d we show JDOS along the line-cut indicated by arrows in Fig. S5a and b. Based on this simulation, we select the integration area between the two circles with $0.13\,\pi/a_{\mathrm{Fe-Fe}} < |q| < 0.55\pi/a_{\mathrm{Fe-Fe}}$, as shown in Figs. S5a and b, and marked by the vertical lines in Fig. S5d. As we can see, the weight given by the three scattering channels shown in Fig. S5c dominate within the area of the two red circles. While the small-q inter- and intra-pocket scatterings contribute weight mainly within the inner circle.
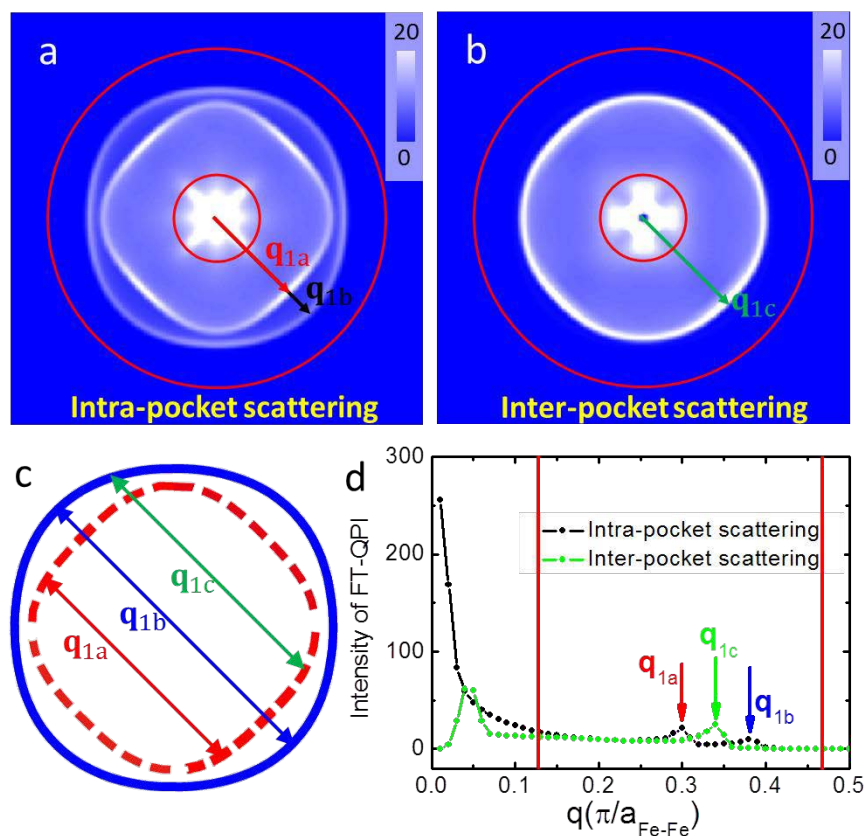
Figure S5 | Selection of the integration area. a, b, The intensities of intra- and inter-pocket scattering obtained by calculating JDOS from the band structure depicted in **c. d,** The simulated joint density for intra- and inter-pocket scattering along the lines indicated by arrows in **a** and **b**.

6. Masking out the effect of a bound state on the integral of $\delta\rho^-$

As shown in Fig. 3b, the impurity bound state induces a large peak around 4 meV in the integral of $\delta\rho^-(\mathbf{q}, E)$, which steals the weight from between the two superconducting gaps at $\Delta_1 \approx 14$ meV and $\Delta_2 \approx 8.5$ meV. However, according to the theoretical proposal[S3], the behavior of $\delta\rho^-(\mathbf{q}, E)$ between the large gap and the small gap is of vital importance for distinguishing between the $s^{\pm}$ and s^{++} pairing. To

get a clear view of the signal between two superconducting gaps, for the conductance mapping measured at the energy in the vicinity of the impurity bound state (3 ~ 5.5 meV), we remove the central part of the dI/dV map within a circle of the radius $R = 3$, about 29 pixels around the impurity, which eliminates the states mostly affected by the impurity bound state; instead, we use inside this circle a parabolic extrapolation of the form $\delta\rho(E) = AE^2 + BE$, where A and B were chosen so as to ensure continuity and smoothness of the resulting dI/dV map. After that, we calculated the integral of $\delta\rho^-(\mathbf{q}, E)$ using the resulting dI/dV map, thus obtaining the data in Fig. 3c.

7. Theoretical calculations including masking out the bound state peak

To facilitate the comparison with the experimental STM data, we employed the multiband T-matrix approach using two parabolic electron bands with the dispersion

$$\varepsilon_\nu(\mathbf{k}) = t\left(\frac{k_x^2}{1\pm\epsilon} + \frac{k_y^2}{1\mp\epsilon}\right) - \mu \quad \text{with} \quad t = 34 \text{ meV}, \quad \epsilon = 0.2 \quad \text{and} \quad \mu = 10.6 \text{ meV}.$$ The scattering of quasiparticles by non-magnetic impurities, measured in the FT-QPI, was calculated as a correction to the local density of states (LDOS), using the standard T-matrix approach describing multiple scattering by a single impurity. Specifically, we compute the correction to the local density of states

$$\delta\rho(E) = \frac{1}{2} \text{Tr Im} \sum_{\mathbf{k},\mathbf{q},\mu,\nu} (\tau_0 + \tau_3) G_\mu^0(k, E)\, t_{\mu\nu}(E) G_\nu^0(k, E) \tag{S1}$$

Here, $G_\mu^0(\mathbf{k}, E) = -\frac{iE\tau_0 + \varepsilon_\mu(\mathbf{k})\tau_3 + \Delta_\mu\tau_1}{E^2 + \Delta_\mu^2 + \varepsilon_\mu^2(\mathbf{k})}$ refers to the Nambu-Gor'kov Green's function for the band μ, τ_i is the i-th Pauli matrix. As in the experiment, we choose the superconducting gaps to be $\Delta_{\text{small}} = 8.5$ meV and $\Delta_{\text{large}} = 14$ meV. The T-matrix in

band and Nambu-Gor'kov space is defined as

$$\hat{t}(E) = \left[1 - \hat{U}\tau_3 \sum_{\mathbf{k}} \hat{G}(\mathbf{k}, E)\right]^{-1} \tau_3 \hat{U}, \qquad (S2)$$

where $U_{\mu\,\mu} = U_{\text{intra}}\tau_0$ and $U_{\mu\,\nu} = U_{\text{inter}}\tau_0$ are the intra- and interband non-magnetic impurity scattering strength, respectively. To be specific, we used the $s^{\pm}$ scenario, and in order to obtain a bound state we used $U_{\text{intra}} = U_{\text{inter}} = 6.8\ t$. Furthermore, for numerical stability we also assumed a quasiparticle damping of $\Gamma = 0.2\Delta_{\text{small}}$. The results for the normal state $\delta\rho(E = 0)$ are shown in Fig. S6b.

As in the experiment, we next compute the anti-symmetrized correction to the local density of states $\delta\rho^{-}(E) = \frac{1}{2}[\delta\rho(E) - \delta\rho(-E)]$ in the superconducting state, following the original proposal of Ref. S3 using the same (s^{++}) and the opposite ($s^{\pm}$) phases of the superconducting order parameters and summing all intraband and interband contributions. As was argued previously[S3], the resulting quantity will be only sensitive to the coherence phase factor and all non-relevant contributions cancel out. The results are shown in Figure S6a for energies up to 20 meV. Clearly the phase structure is strongly visible in the energy interval $\Delta_{\text{small}} < E < \Delta_{\text{large}}$. To exclude the effect of the impurity bound state, which occurs for the s$^{\pm}$ case at $U_{\text{intra}} = U_{\text{inter}}$, we masked the bound state in real space by using in its stead the same parabolic extrapolation employed in the experimental analysis, denoted by the thin blue curve, so that the resulting function is continuous and smooth. A similar procedure was applied to the experimental data, as described in the next section.
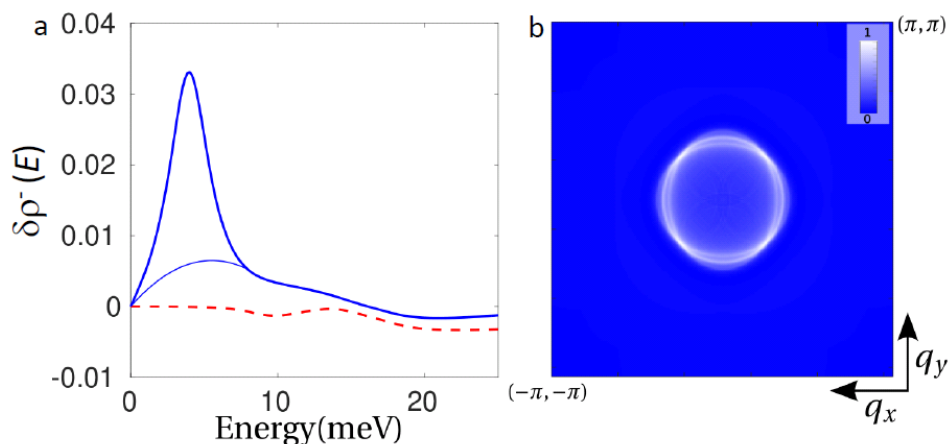
Figure S6 | Theoretical modelling of the STM data. **a**, Anti-symmetrized **k**-integrated correction to the local density of states for the s^{++} (red dashed curve) and $s^{\pm}$ (blue solid thick curve) scenarios. The thin blue curve corresponds to the $s^{\pm}$ case with parabolic masking of the resonant bound state in real space as $\delta\rho(E) = AE^2 + BE$ with A = -0.213x10^{-3} states/meV^3 and B = 2.354x10^{-3} states/meV^2 as described in the text. **b**, The normal state local density of states for $E = 0$.

8. Control experiments

We repeated the measurements on the same impurity in Fig. 1a about two weeks later. Probably due to the slightly changed state of the tip, the image (Fig. S7) was slightly different from the original state, but the qualitative features do not change. We then studied another isolated impurity (Fig. S8). In both cases, we re-calculated $\delta\rho^-(E)$ using the same algorithm described above and obtained results similar to those in Fig. 3b, c. These two control experiments are now described in more detail.

Figure S7a shows the measured image in the control experiment around the same impurity shown in Fig. 1a. The tunneling spectrum measured far away from the

impurity shows similar superconducting gap values as indicated in the inset of Fig. 1b, and, most importantly, the peak energy of the impurity bound state is still around 4.0 meV. The condition of the tip is still good, as shown by the atomic resolution of the topography and the observation of clear superconducting coherence peaks in the tunneling spectrum. We measured the dI/dV map around the impurity and calculated $\delta\rho^-(E)$ following the same procedures. The results are shown in Figs. S7c and d. We can see that the output are similar to that in Figs. 3b and c.
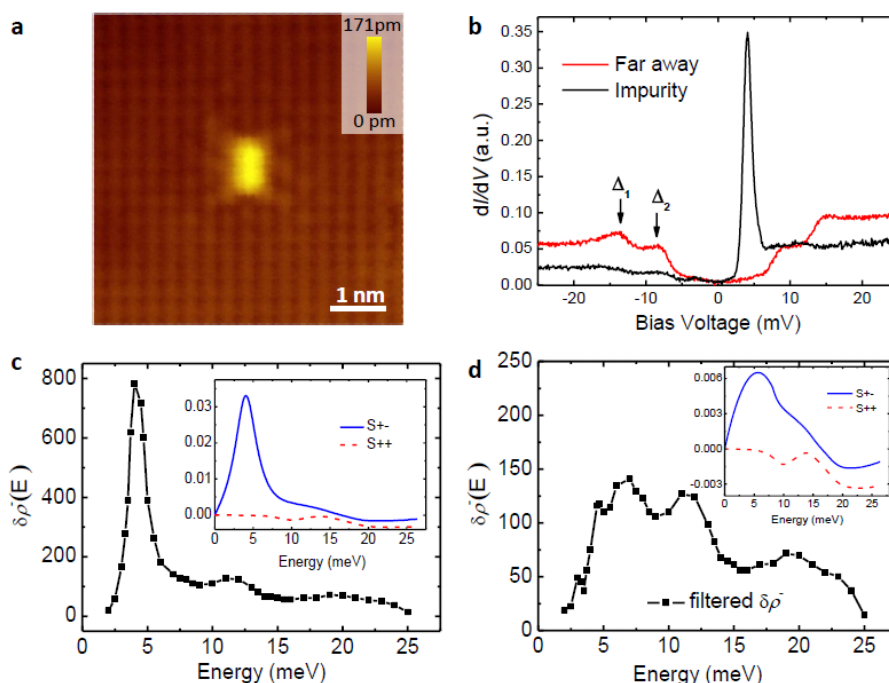

Figure S7 | Control experiment on the same impurity in Fig.1a in two weeks after the initial measurement. a, The topography around the impurity is measured with V_{bias} = 30 mV and I_t = 100 pA. The color bar represents height of the background with unit of pico-meter. **b,** The spectra measured at the center of the impurity and far away from the impurity. The energy of the impurity bound state is 4.0 meV, which is

consistent with the original case shown in Fig. 1b. **c,** The calculated $\delta\rho^-(E)$ versus E.

d, The calculated $\delta\rho^-(E)$ after masking out the impurity state peak. The insets in **c**

and **d** show the theoretical calculations for the corresponding cases.

As a second control experiment, we chose another isolated impurity in the same

sample, the topography for which is shown in Fig. S8a. Interestingly, this impurity has

two resonant peaks with peak energies of about 2.7 meV and 5.6 meV, and both

peaks do not shift with the applied magnetic field of 11 T (Fig. S8b). We assume that

this impurity is non-magnetic, for the reasons stated in the text. We again performed

QPI measurements around the impurity and calculated $\delta\rho^-(E)$. The result is shown

in Fig. S8c; in this case, there are two closely spaced peaks in $\delta\rho^-(E)$, possibly due

to the different local environment of this defect. After masking out the resonances in

the density of states mapping and performing the integration, we get $\delta\rho^-(E)$ which

is shown in Fig. S8d. One can see that the output is very similar to that in Figs. S7d
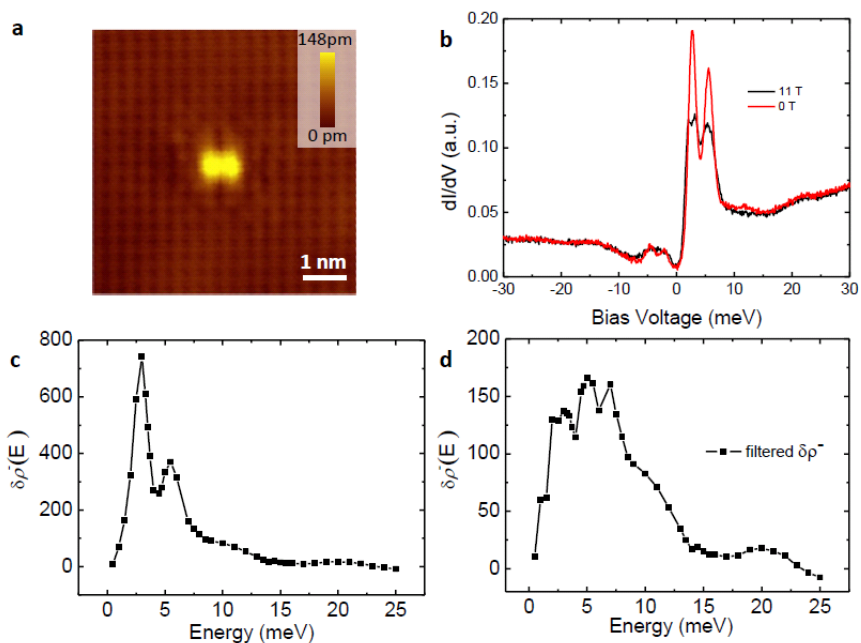
and 3c.

Figure S8 | Control experiment on another impurity. a, The STM topography measured with V_{bias} = 30 mV and I_t = 100 pA. **b,** Tunneling spectra measured at the defect under B = 0 T and 11 T, respectively. The impurity resonances occur at energies of 2.7 meV and 5.6 meV. The magnetic field does not shift the resonance energies, indicating the non-magnetic character of this impurity. **c,** Integral of $\delta\rho^-(E)$ as a function of E. The calculation method of $\delta\rho^-(E)$ is the same as that used in the main text of the paper. **d,** The calculated $\delta\rho^-(E)$ after masking out the impurity resonances.

In summary, the experiment and analysis can be reproduced under differing conditions; we thus conclude that our result indicating sign-changing superconducting gaps in $(Li_{1-x}Fe_x)OHFe_{1-y}Zn_ySe$ is robust and convincing.

References

S1. Li, W. *et al*. Phase separation and magnetic order in K-doped iron selenide superconductor. *Nat. Phys.* **8**, 126-130 (2012).

S2. Sprau, P. O. *et al*. Discovery of Orbital-Selective Cooper Pairing in FeSe. *Science* **357**, 75-80 (2017).

S3. Hirschfeld, P. J., Altenfeld, D., Eremin, I. & Mazin, I. I. Robust determination of superconducting gap sign changes via quasiparticle interference. *Phys. Rev. B* **92**, 184513 (2015).